AD-A052 414   OHIO STATE UNIV COLUMBUS ELECTROSCIENCE LAB   F/G 20/14
BACKSCATTER OF A LARGE ROTATING CONDUCTING CYLINDER WITH ARBITR--ETC(U)
FEB 78 C W CHUANG, A A KSIENSKI   AFOSR-74-2611
UNCLASSIFIED   ESL-783815-4   AFOSR-TR-78-0687   NL

| OF |
AD
A052414

END
DATE
FILMED
5-78
DDC

ADA052414

AD No.
DDC FILE COPY

BACKSCATTER OF A LARGE ROTATING CONDUCTING CYLINDER
WITH ARBITRARY CROSS SECTION

C.W. Chuang
A.A. Ksienski
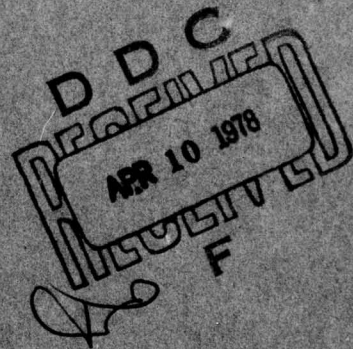
The Ohio State University

ElectroScience Laboratory

Department of Electrical Engineering
Columbus, Ohio   43212

D D C
APR 10 1978
F

NOTICES

When Government drawings, specifications, or other data are used for any purpose other than in connection with a definitely related Government procurement operation, the United States Government thereby incurs no responsibility nor any obligation whatsoever, and the fact that the Government may have formulated, furnished, or in any way supplied the said drawings, specifications, or other data, is not to be regarded by implication or otherwise as in any manner licensing the holder or any other person or corporation, or conveying any rights or permission to manufacture, use, or sell any patented invention that may in any way be related thereto.

REPORT DOCUMENTATION PAGE		READ INSTRUCTIONS BEFORE COMPLETING FORM
1. REPORT NUMBER AFOSR-TR- 78- 0687	2. GOVT ACCESSION NO.	3. RECIPIENT'S CATALOG NUMBER
4. TITLE (and Subtitle) BACKSCATTER OF A LARGE ROTATING CONDUCTING CYLINDER WITH ARBITRARY CROSS SECTION		5. TYPE OF REPORT & PERIOD COVERED Interim rept. 6. PERFORMING ORG. REPORT NUMBER 783815-4
7. AUTHOR(s) C. W. Chuang A. A. Ksienski		8. CONTRACT OR GRANT NUMBER(s) AFOSR-74-2611
9. PERFORMING ORGANIZATION NAME AND ADDRESS Ohio State University Department of Electrical Engineering Columbus, Ohio 43212		10. PROGRAM ELEMENT, PROJECT, TASK AREA & WORK UNIT NUMBERS 61102F 2304/A2
11. CONTROLLING OFFICE NAME AND ADDRESS Air Force Office of Scientific Research/NM Bolling AFB, Washington, DC 20332		12. REPORT DATE Feb 78 13. NUMBER OF PAGES 29 34 p.
14. MONITORING AGENCY NAME & ADDRESS(if different from Controlling Office) ESL-783815-4		15. SECURITY CLASS. (of this report) UNCLASSIFIED 15a. DECLASSIFICATION/DOWNGRADING SCHEDULE

16. DISTRIBUTION STATEMENT (of this Report)

Approved for public release; distribution unlimited.

17. DISTRIBUTION STATEMENT (of the abstract entered in Block 20, if different from Report)

18. SUPPLEMENTARY NOTES

19.

Radam Phenomenon
Rotating Cylinder
Modulation
Backscatter Power Density Spectrum

Fast Fourier Transform
Geometrical Theory of Diffraction

20. ABSTRACT (Continue on reverse side if necessary and identify by block number)

   A quasi-stationary method in conjunction with GTD (geometrical theory of diffraction) techniques is used for calculating the backscattered field from a large rotating conducting cylinder with arbitrary cross section. Using this method, the scattered field at each time t is obtained as if the cylinder were stationary. The power density spectrum is then obtained using Fourier transformation. The backscatter power density spectrum of a large rotating cylinder

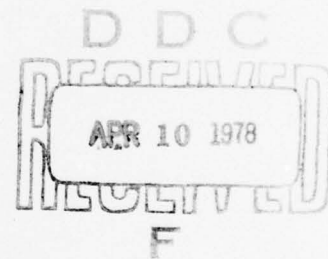DD FORM 1473 EDITION OF 1 NOV 65 IS OBSOLETE
1 JAN 73

402 251

20. Abstract

consists of discrete spectral lines. For an orthogonal polygon-cylinder, the backscatter power density spectrum is symmetric about the incident frequency. A modal expansion solution is also obtained for verifying the results obtained by using GTD techniques.

TABLE OF CONTENTS

I. INTRODUCTION

Electromagnetic scattering from a moving body generally is a very difficult problem to solve. Due to the motion of the scatterer, the constitutive parameters, μ, ε and σ are not only functions of position but also functions of time, thus introducing modulation in the scattered fields. To make things worse, the boundary conditions for a moving body are much more complicated than those encountered in problems involving stationary bodies only [1]. These are probably the main roadblocks to obtaining the solutions of the scattering problems involving moving bodies.

However, in some cases, approximate solutions of the scattering problems involving moving bodies can be obtained. In this report we shall discuss the backscatter of a large rotating conducting cylinder. Approximate solutions of the backscatter will be obtained using the quasi-stationary method. The investigation of this problem stems from the current interest in the DADAM phenomena which involve the identification of moving vehicles based on the characteristic modulations that they impose on their radar returns.

II. FORMULATION AND NUMERICAL SOLUTIONS

An infinitely long conducting cylinder is rotating at an angular velocity α about its axis. A plane wave is incident normally upon the cylinder. Due to the rotation of the cylinder, the constitutive parameters are then periodic functions of time with period T. For a cylinder with arbitrary cross-section, $T = 2\pi/\alpha$. However, for an orthogonal polygon-cylinder, $T = 2\pi/N\alpha$, where N is the number of sides of the polygon. Assume that $1/T$ is much smaller than the frequency of the incident wave. Then the backscatter is both amplitude and phase modulated which can be written as

$$\overline{E}_s = \overline{\Sigma}(t)\, e^{j\omega_0 t} \quad , \tag{1}$$

where ω_0 is the incident angular frequency and $\overline{\Sigma}(t)$ is a complex function of t with period T. Because of the assumption, $2\pi/T << \omega_0$, the negative frequency components of the Fourier transform of $\overline{E}_s$ will be negligible. Therefore $\overline{E}_s$ can be considered as an analytic signal.

An exact solution of $\overline{\Sigma}(t)$ can be obtained in two ways. The first is to solve the scattering problem in the time domain using boundary conditions for moving bodies. The second involves transformations from the laboratory frame to a non-inertial frame which is corotating with the cylinder. Both methods are very tedious and solutions difficult to obtain. However, under the assumptions that $\omega_0 >> 2\pi/T$ and that the linear velocity of the cylinder ($v = a\alpha$, a = the largest radius) is much smaller than the velocity of light in vacuum, an approximate solution of $\overline{\Sigma}(t)$ can be much easily obtained using the quasi-stationary method. Using this

1

method, the backscatter $\overline{\Sigma}(t)$ at each time t is obtained as if the cylinder were stationary. The ordinary frequency domain techniques and the boundary conditions for stationary bodies can then be applied to solve the problem. The inequalities $\omega_0 >> 2\pi/T$ and $c >> a\alpha$ are easily satisfied with high incident frequency and low rotating velocity. Thus the quasi-stationary method can be employed in many practical situations.

In applying the quasi-stationary method, GTD (geometrical theory of diffraction) techniques can be employed for solving $\overline{\Sigma}(t)$ from a large conducting cylinder. In the following, we shall first briefly review the GTD techniques pertinent to this problem. For a more detailed formulation readers are referred to a paper by Wang* [2].

As shown in Figure 1, a conducting convex cylinder is illuminated by a line source. The cylinder is modeled as a polygonal cylinder with N flat faces. The line source illuminates the polygonal cylinder giving
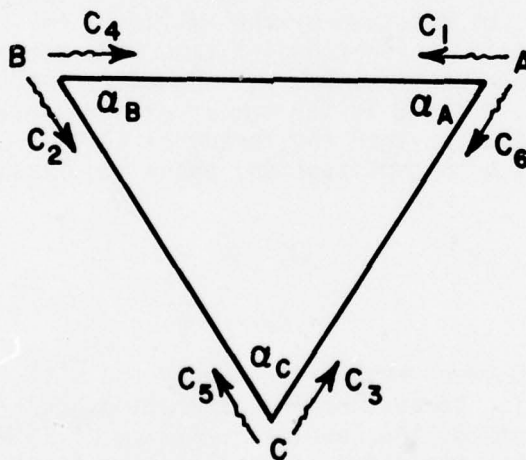
LINE SOURCE
●

Figure 1. The self-consistent representation of the surface waves traveling on the triangular cylinder.

---

rise to reflected fields and edge-diffracted fields, which consist of singly- and multiply-diffracted fields. The multiply-diffracted rays are due to those surface waves traveling, at least once, along the surface of the polygonal cylinder and then diffracting from the edges of the polygon. The surface waves on each side of the polygon are conveniently combined into two such waves traveling in opposite directions. Hence there are totally 2N surface waves on a polygonal cylinder with N sides. The amplitudes of these surface waves need be solved first. We shall use the triangular cylinder of Figure 1 as an example to set up equations for solving these amplitudes.

In Figure 1 the C_i are the unknown amplitudes of the surface waves on the polygon faces. The surface wave field is defined as

$$U(\rho) = C_i \frac{e^{-jk\rho}}{\sqrt{\rho}} \quad , \tag{2}$$

where $k = \omega_0/c$, and ρ is the distance from the caustic of the surface wave to the field point. This field equation is not valid at the caustic. The boundary condition at the corners may be expressed as follows:

at corner A,

$$C_1 = C_3 T_{CA} + C_4 R_{BA} + V_1 \quad , \tag{3}$$

$$C_6 = C_4 T_{BA} + C_3 R_{CA} + V_6 \quad , \tag{4}$$

at corner B,

$$C_2 = C_1 T_{AB} + C_5 R_{CB} + V_2 \quad , \tag{5}$$

$$C_4 = C_5 T_{CB} + C_1 R_{AB} + V_4 \quad , \tag{6}$$

at corner C,

$$C_3 = C_2 T_{BC} + C_6 R_{AC} + V_3 \quad , \tag{7}$$

$$C_5 = C_6 T_{AC} + C_2 R_{BC} + V_5 \quad . \tag{8}$$

Equations (3) - (8) can be written in matrix form,

$$[Z](C) = (V) \quad , \tag{9}$$

where $[Z]$ is the coupling matrix and (V) is the excitation column.

The coupling matrix $[Z]$ is unsymmetric. Its elements specify the interactions among the surface waves. The diagonal elements are $Z_{ii}=1$. The other elements are 0, T_{xy} or R_{xy}. The transmission coefficient T_{xy} and the reflection coefficient R_{xy} are given by

3

$$T_{xy} = \frac{e^{-jk\rho_{xy}}}{\sqrt{\rho_{xy}}} \quad \frac{1}{2} \quad D_{\substack{s \\ h}}(360°-\alpha_y, 0°, 90°) \quad , \tag{10}$$

$$R_{xy} = \frac{e^{-jk\rho_{xy}}}{\sqrt{\rho_{xy}}} \quad \frac{1}{2} \quad D_{\substack{s \\ h}}(0°, 0°, 90°) \quad , \tag{11}$$

where ρ_{xy} is the distance between the corners X and Y, α_y is the wedge angle for corner Y and $D_{\substack{s \\ h}}(\phi, \phi', \beta_0)$ is the scalar wedge diffraction coefficient given by Kouyoumjian and Pathak [3].

The elements of the excitation column (V) relate the source excitations to the surface waves on the polygon surfaces. The typical element of (V) is given by

$$V_x = \frac{e^{-jk\rho_{sx}}}{\sqrt{\rho_{sx}}} \quad D_{\substack{s \\ h}}(0°, \phi', 90°) \quad , \tag{12}$$

where ρ_{sx} is the distance between the source and corner X. However, when a corner is not directly illuminated by the source, the excitation element associated with that corner is 0. Furthermore, for the TM case, the diffraction coefficient D_s in Equation (12) is identically zero and should be replaced by its normal derivative [2].

From the matrix equation, Equation (9), we obtain the amplitudes of the surface waves on the polygon surfaces. The scattered field at an observation point P is equal to the sum of the fields associated with all the rays emanating from the cylinder and passing through P:

$$U(P) = \sum_{\text{rays}} U_n(P) \quad , \tag{13}$$

which includes the reflected field and the diffracted field. Referring to Figure 2, the reflected field associated with the reflected ray $\overline{S'P}$ emanating from the image S' is given as

$$U^r_{S'P} = \pm \frac{e^{-jk\rho_{S'P}}}{\sqrt{\rho_{S'P}}} \quad , \tag{14}$$

where the positive sign is for the Neumann (hard) boundary condition associated with the magnetic line source, and the negative sign is for the Dirichlet (soft) boundary condition associated with the electric
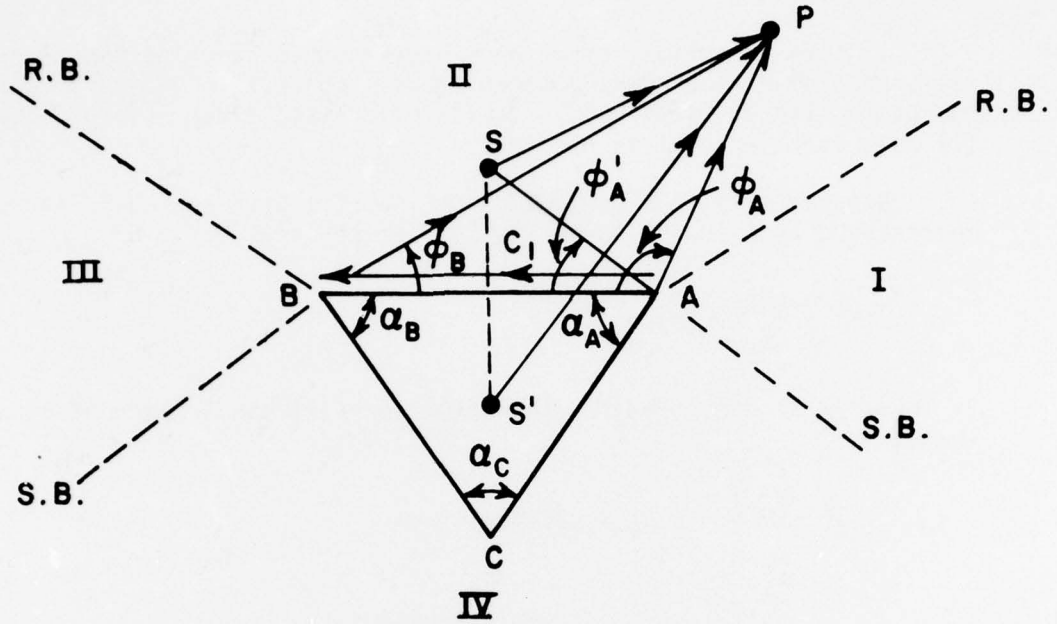
Figure 2.   Direct ray $\overrightarrow{SP}$, reflected ray $\overrightarrow{S'P}$, singly-
diffracted ray $\overrightarrow{SAP}$, and surface-wave
diffracted ray $\overrightarrow{ABP}$.

line source.   The singly-diffracted field associated with the ray $\overrightarrow{SAP}$
is given by

$$U_{SAP}^{d} = \frac{e^{-jk\rho_{SA}}}{\sqrt{\rho_{SA}}} \; D_{s \atop h}(\phi_A, \phi_A', 90°) \; \frac{e^{-jk\rho_{AP}}}{\sqrt{\rho_{AP}}} \qquad , \qquad (15)$$

and the surface-wave-diffracted field associated the surface wave C_1 is
given by

$$U_{ABP}^{sd} = C_1 \; \frac{e^{-jk\rho_{AB}}}{\sqrt{\rho_{AB}}} \; \frac{1}{2} D_{s \atop h}(\phi_B, 0°, 90°) \; \frac{e^{-jk\rho_{BP}}}{\sqrt{\rho_{BP}}} \qquad . \qquad (16)$$

These fields, Equations (14), (15) and (16), exist only in their illumi-
nated regions.   In the shadowed regions the corresponding fields vanish.
Summing the reflected fields, the singly-diffracted fields and the sur-
face-wave-diffracted fields, we then obtain the scattered field at P.
This field depends on the orientation of the polygonal cylinder.   As the
cylinder rotates, the scattered field at P, i.e., U(P), then varies with

5

time. Therefore one may write U(P) as U(P,t) which is essentially equivalent to $\Sigma(t)$ of Equation (1). A computer program is written for calculating U(P,t) (or $\Sigma(t)$).

In this investigation we are interested in studying the power density spectrum of the backscattered field. The power density spectrum of the backscattered field can be easily calculated after $\overline{\Sigma}(t)$ of Equation (1) as a function of t is obtained.

Because $\overline{\Sigma}(t)$ is a periodic function of t with period T, it can be represented as a summation of its Fourier series,

$$\overline{\Sigma}(t) = \sum_{m=-\infty}^{\infty} \overline{F}(m) \, e^{j2\pi mt/T} \qquad . \tag{17}$$

If $|\overline{F}(m)| \approx 0$, for $|m| \geq N_0/2$, then Equation (17) can be adequately approximated by

$$\overline{\Sigma}(t) = \sum_{m=-N_0/2}^{N_0/2-1} \overline{F}(m) \, e^{j2\pi mt/T}$$

$$= \sum_{m=0}^{N_0-1} \overline{F}(m-N_0/2) \, e^{j2\pi(m-N_0/2)t/T} \qquad . \tag{18}$$

Let

$$\overline{\Sigma}(t) \, e^{j\pi N_0 t/T} = \overline{\Sigma}_1(t) \qquad , \tag{19}$$

and

$$\overline{F}(m-N_0/2) = \overline{F}_1(m) \qquad . \tag{20}$$

Then

$$\overline{\Sigma}_1(t) = \sum_{m=0}^{N_0-1} \overline{F}_1(m) \, e^{j2\pi mt/T} \qquad . \tag{21}$$

The inverse transform is

$$\overline{F}_1(m) = \frac{1}{N_0} \sum_{tN_0/T=0}^{N_0-1} \overline{\Sigma}_1(t) \, e^{-j2\pi mt/T} \qquad . \tag{22}$$

6

Equation (22) can be solved using FFT programs.

From Equations (1) and (17), we have

$$\overline{E}_S = \sum_{m=-\infty}^{\infty} \overline{F}(m) \, e^{j(\omega_0 + 2\, m/T)t} \qquad . \qquad (23)$$

The power density spectrum of Equation (23) is defined by [4]

$$S(\omega) = \frac{1}{2T_0} \left| \int_{-T_0}^{T_0} \sum_{m=-\infty}^{\infty} \overline{F}(m) \, e^{j[(\omega-\omega_0)-2\pi m/T]t} \, dt \right|^2$$

$$= \frac{2}{T_0} \sum_{m=-\infty}^{\infty} \overline{F}(m) \, \frac{\sin[(\omega-\omega_0)-2\pi m/T]T_0}{(\omega-\omega_0)-2\pi m/T}$$

$$\cdot \sum_{m'=-\infty}^{\infty} \overline{F}*(m') \, \frac{\sin[(\omega-\omega_0)-2\pi m'/T]T_0}{(\omega-\omega_0)-2\pi m'/T} \qquad . \qquad (24)$$

As $T_0 \to \infty$

$$S(\omega) = 2\pi \sum_{m=-\infty}^{\infty} |\overline{F}(m)|^2 \, \delta[(\omega-\omega_0)-2\pi m/T] \qquad . \qquad (25)$$

Thus the power density spectrum of the scattered field from a rotating cylinder consists of spectral lines located at

$$\omega = \omega_0 + 2\pi m/T = \omega_0 + mN\alpha \quad , \quad m=0,\pm 1,\pm 2,\cdots \; . \qquad (26)$$

Figures 3 to 10 show some power density spectra of the backscattered fields from a large rotating conducting cylinder. The cross-section of the cylinder is an N-sided orthogonal polygon. The spectra in Figures 3 and 4 are set to 0 dB at m=0 ($\omega=\omega_0$). The dB values of the spectra in other figures are then adjusted relative to these two spectral lines. Examining these figures, we note several interesting features:

(1) The spectrum is symmetric about m=0. This property is due to the symmetry possessed by the scattering orthogonal polygon-cylinder. In the next section, we shall show that the power density spectrum of the backscattered field from a rotating cylinder with an arbitrary cross-section in general does not have this symmetry property.
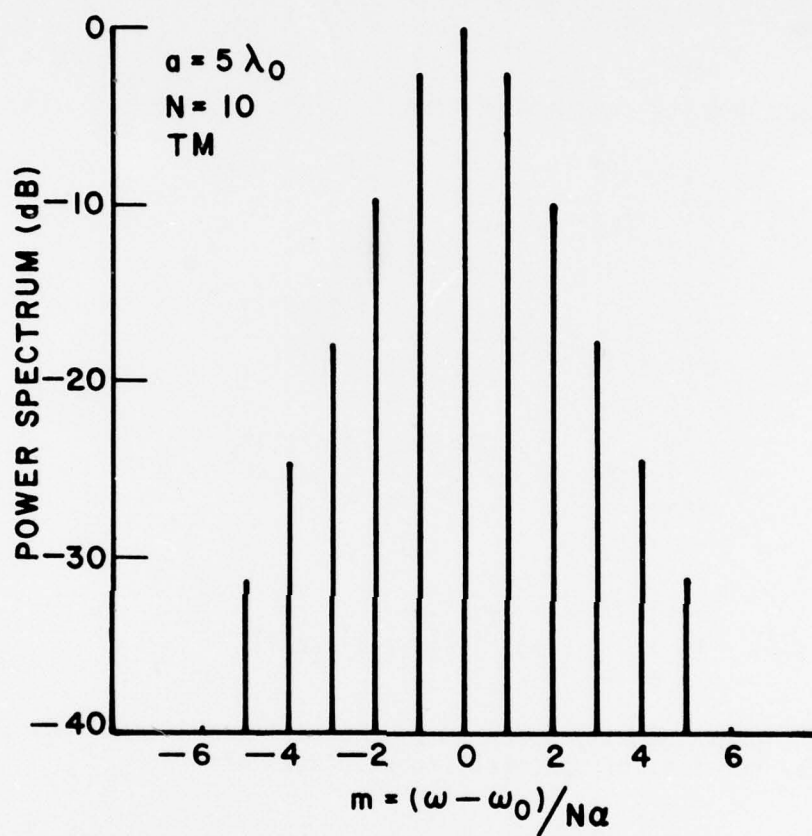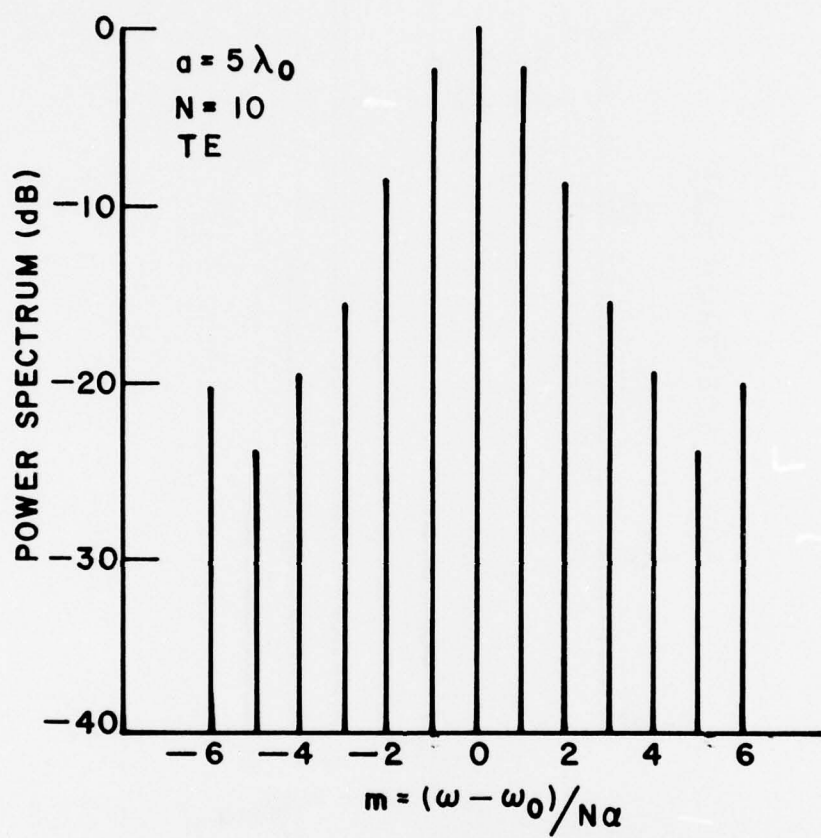
7

Figure 3.   Power density spectrum

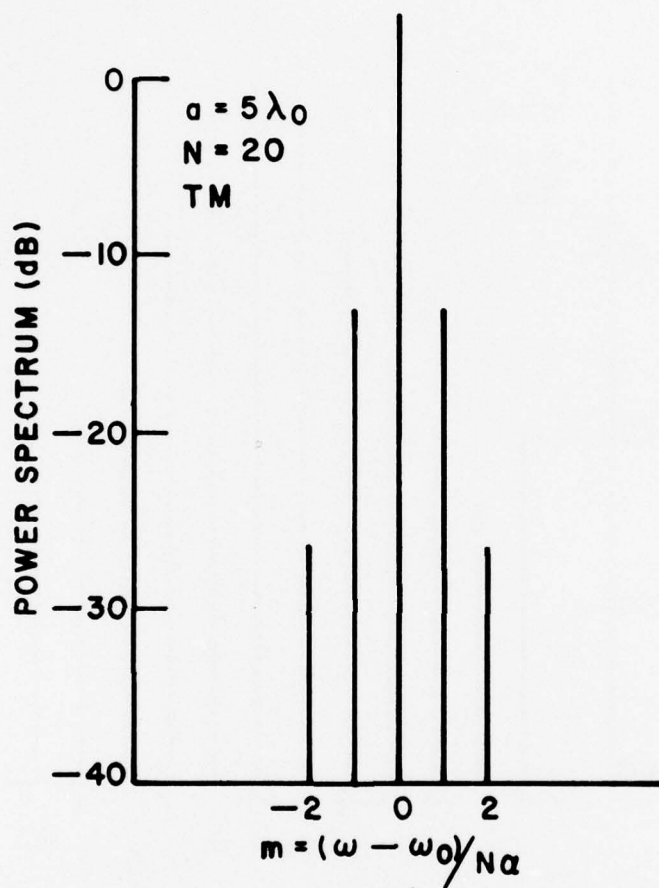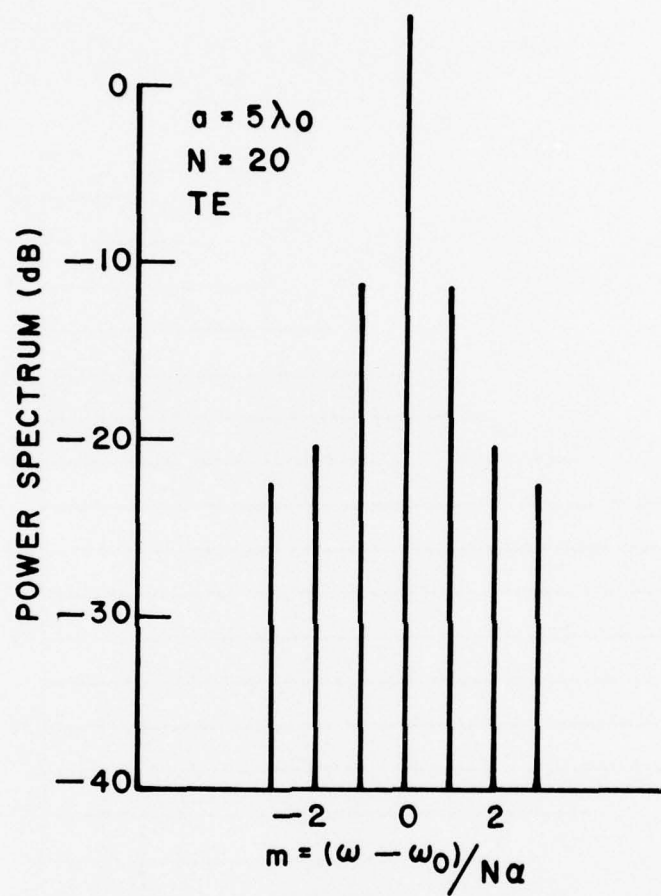Figure 4.   Power density spectrum.

9

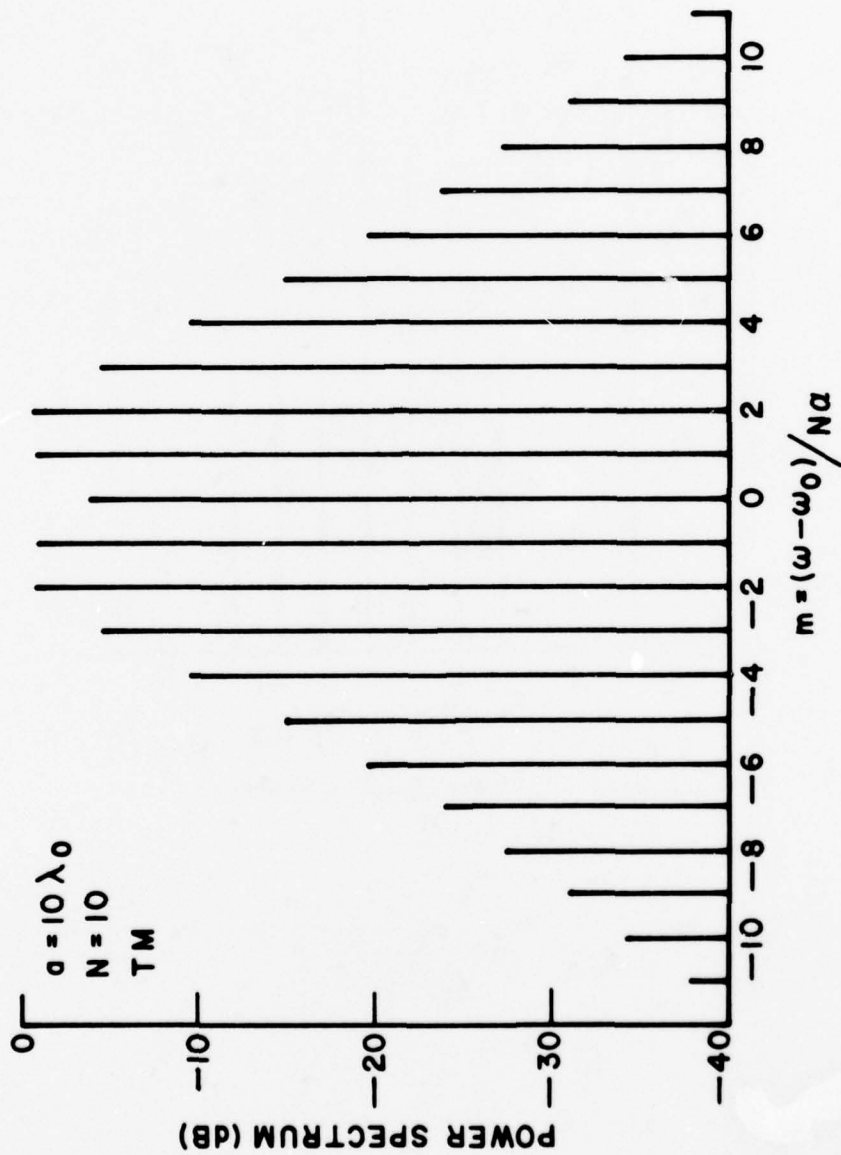Figure 5. Power density spectrum.

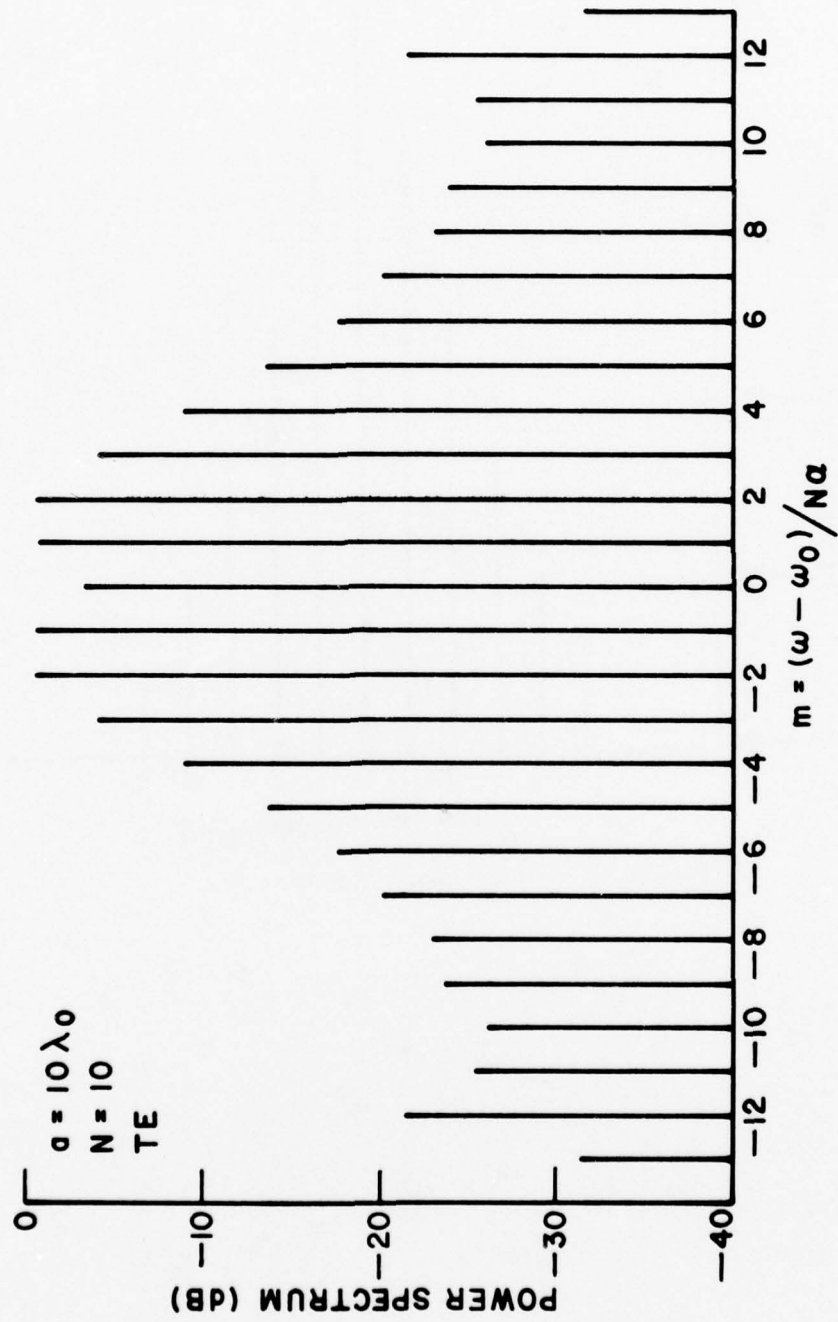Figure 6. Power density spectrum.

Figure 7. Power density spectrum.
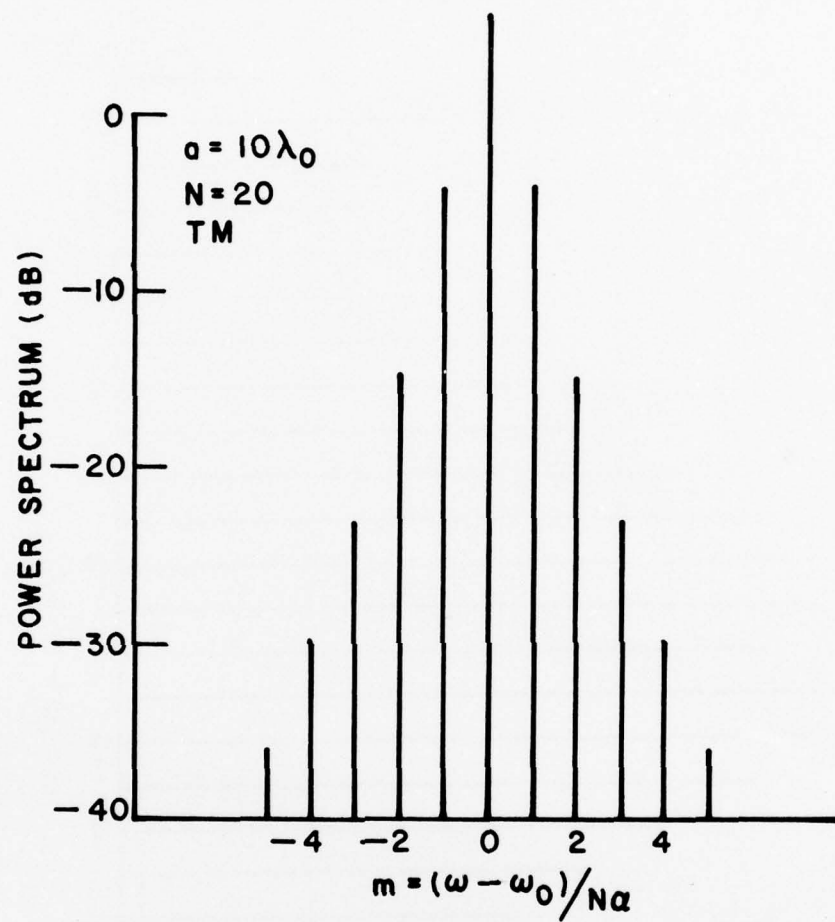
Figure 8. Power density spectrum.

13

Figure 9. Power density spectrum.
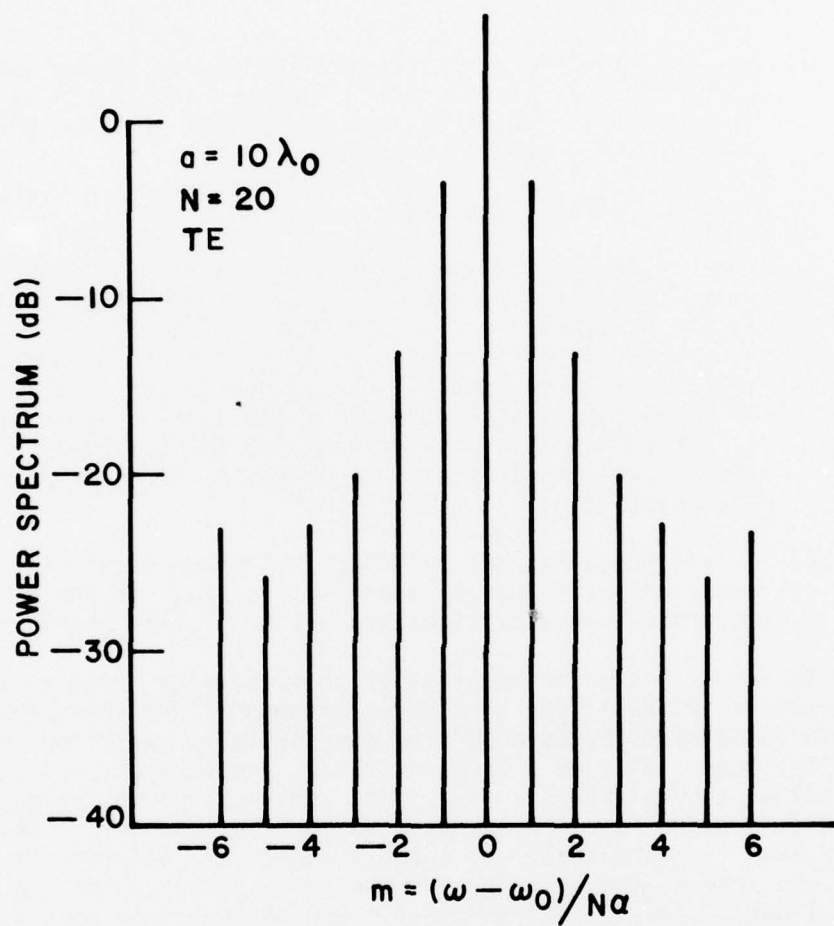
Figure 10.   Power density spectrum.

(2) The spectrum at m=0 is not always a maximum as evidenced
     from Figures 7 and 8. This is probably true when the length
     of the polygon side exceeds several times of the incident
     wavelength.

(3) As $|m|$ increases, the spectrum usually decreases monotonically
     and faster for the TM case. However, for the TE case the
     spectrum has a local maximum around $|m| \approx \omega_D/N\alpha$, where ω_D is
     the Doppler angular frequency given by

$$\omega_D = 2\pi \cdot 2a\alpha/\lambda_0 = 2a\alpha\omega_0/c \qquad , \qquad\qquad (27)$$

     where a and $a\alpha$ are the largest radius and the largest linear
     velocity of the cylinder, respectively. For example, in
     Figure 4, $\omega_D \approx 20\pi\alpha$ and a local maximum occurs at $|m| = 6$
     $\approx \omega_D/N\alpha$. The differences in the shapes of the spectra in
     the TM and TE cases are probably due to the fact that in the
     TM case, the induced current on the surface of the cylinder
     is perpendicular to the velocity of the cylinder, while in
     the TE case the induced current has a component parallel to
     the velocity.

(4) In all these figures, although not shown explicitly, the
     spectrum drops sharply when $|m| > \omega_D/N\alpha$. In the next section,
     we present an analytical evaluation of this phenomenon.

Figures 3-10 are the backscatter power density spectrum when a
plane wave is incident upon a rotating orthogonal polygon-cylinder.
They can be obtained by using a line current $10^4\lambda_0$ away from the center
of the cylinder. At such a large distance, the curvature of the incident
wavefront at the cylinder is very small and the incident wave can be con-
sidered as a plane wave. However, when the line current is only $100\lambda_0$
or less away from the center of the cylinder, the line current is in the
near-field zone of the cylinder and the wave incident upon the cylinder
is a cylindrical wave. The monostatic scattering power density spectra
when the line current is $25\lambda_0$, $50\lambda_0$ and $100\lambda_0$ away from the center of the
cylinder are found to be essentially the same as those shown in Figures 3
to 10. Thus the power density spectra of a rotating cylinder can be ob-
tained using near-field measurements.

III. ANALYTICAL APPROACH

Numerical solutions reveal some interesting properties of the power
density spectrum of the backscattered field from a large rotating cylin-
der. In this section we shall investigate this problem analytically to
further substantiate the results established from numerical solutions
presented in the last section.

The vector potential due to a current source $\bar{J}(\bar{r},t)$ is given by

16

$$\overline{A}(\overline{r},t) = \frac{\mu_0}{4\pi} \iint \frac{\overline{J}(\overline{r}',t')}{R} \delta(t'+R/C-t) \, dx'dy'dz'dt' \qquad , \qquad (28)$$

where $R = |\overline{r}-\overline{r}'|$ and δ is a Dirac delta function. Taking the Fourier transform of Equation (28),

$$\overline{A}(\overline{r},\omega) = \frac{\mu_0}{4\pi} \iint \frac{\overline{J}(\overline{r}',t')}{R} e^{-j\omega(t'+R/c)} \, dx'dy'dz'dt' \qquad . \qquad (29)$$

In the two dimensional problem considered here, $\overline{J}(\overline{r}',t')$ is independent of z'. Therefore performing the integration over z' in Equation (29), we obtain

$$\overline{A}(\overline{\rho},\omega) = \frac{\mu_0}{4j} \iint \overline{J}(\overline{\rho}',t') \, H_0^{(2)}(\omega R_1/c) e^{-j\omega t'} \, dx'dy'dt' \qquad , \qquad (30)$$

where $R_1 = |\overline{\rho}-\overline{\rho}'|$ and $H_0^{(2)}$ is a Hankel function of the second kind. In deriving Equation (30), use has been made of the identity

$$\int_{-\infty}^{\infty} \frac{e^{-jkR}}{4\pi R} \, dz' = \frac{H_0^{(2)}(kR_1)}{4j} \qquad , \qquad (31)$$

with $R = [R_1^2 + (z-z')^2]^{1/2}$. In the far field, Equation (30) becomes

$$\overline{A}(\overline{\rho},\omega) = \frac{\mu_0 e^{-j\pi/4} e^{-j\omega\rho/c}}{\sqrt{8\pi\omega\rho/c}} \iint \overline{J}(\overline{\rho}',t') \, e^{-j\omega(t'-\hat{\rho}\cdot\overline{\rho}'/c)} \, dx'dy'dt',$$
$$(32)$$

where $\hat{\rho}$ is a unit vector along $\overline{\rho}$.

Now let $\overline{J}(\overline{\rho},t)$ be the induced current on the rotating cylinder. Then from the vector potential we obtain the scattered electric and magnetic fields. In the TM case, the scattered electric field has only the z-component.

$$E_z(\overline{\rho},\omega) = \frac{-j\omega\mu_0 e^{-j\pi/4} e^{-j\omega\rho/c}}{\sqrt{8\pi\omega\rho/c}} \iint J_z(\overline{\rho}',t') e^{-j\omega(t'-\hat{\rho}\cdot\overline{\rho}'/c)} dx'dy'dt' \quad .$$
$$(33)$$

And in the TE case, the scattered magnetic field has only the z-component,

$$H_z(\overline{\rho},\omega) = \frac{-j\omega e^{-j\pi/4} e^{-j\omega\rho/c}}{c\sqrt{8\pi\omega\rho/c}} \iint [\hat{\rho}\times\overline{J}(\overline{\rho}',t')]_z \, e^{-j\omega(t'-\hat{\rho}\cdot\overline{\rho}'/c)}$$
$$dx'dy'dt' \quad .$$
$$(34)$$

17

The factors outside the integrals in Equations (33) and (34) will be designated as T_M and T_E, respectively.

We shall evaluate the integrations in Equations (33) and (34) by transforming the coordinate system $(\bar{\rho}, t)$ to the coordinate system $(\bar{\rho}_1, t_1)$ which is corotating with the cylinder. The coordinate transformation is governed by the following relations

$$x = x_1 \cos\alpha t_1 - y_1 \sin\alpha t_1 \quad ,$$

$$y = x_1 \sin\alpha t_1 + y_1 \cos\alpha t_1 \quad , \tag{35}$$

$$t = t_1 \quad .$$

These equations can be derived by referring to Figure 11. The jacobian of the transformation is unity. Therefore Equations (33) and (34) become

$$E_z(\bar{\rho}, \omega) = T_M \iint J_z(\bar{\rho}_1', t_1') \, e^{-j\omega(t_1' - \hat{\rho} \cdot \bar{\rho}_1'/c)} \, dx_1' dy_1' dt_1' \quad , \tag{36}$$

and

$$H_z(\bar{\rho}, \omega) = T_E \iint [\hat{\rho} \times \bar{J}(\bar{\rho}_1', t_1')]_z \, e^{-j\omega(t_1' - \hat{\rho} \cdot \bar{\rho}_1'/c)} \, dx_1' dy_1' dt_1' \quad . \tag{37}$$
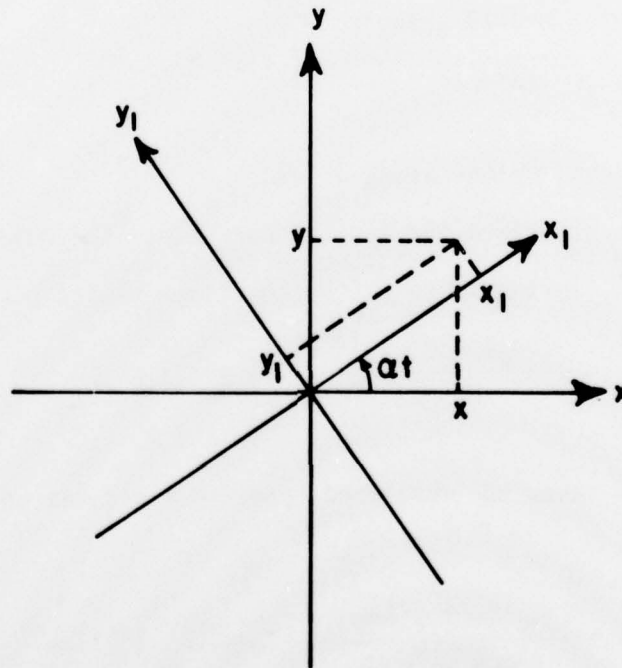

Figure 11. Transformation of coordinates.

18

To proceed, we assume that the incident plane wave has the form $\exp[j\omega_0(t-x/c)]$, which, if written in the corotating frame, becomes

$$\exp\{j\omega_0[t_1-(x_1\cos\alpha t_1 - y_1\sin\alpha t_1)/c]\}$$

$$= \exp\{j\omega_0[t_1-\rho_1\cos(\alpha t_1+\phi_1)/c]\}$$

$$= e^{j\omega_0 t_1}\sum_{k=-\infty}^{\infty} j^{-k} J_k(\omega_0\rho_1/c) e^{jk(\alpha t_1+\phi_1)} \tag{38}$$

where $\rho_1 = (x_1^2 + y_1^2)^{1/2}$, $\phi_1 = \tan^{-1}(y_1/x_1)$, and J_k is a Bessel function. In deriving Equation (38), use has been made of the relation

$$e^{jx\sin\phi} = \sum_{k=-\infty}^{\infty} J_k(x) e^{jk\phi} \tag{39}$$

In view of Equation (38), the induced current $\overline{J}(\overline{\rho}_1,t_1)$ can be written as

$$\overline{J}(\overline{\rho}_1,t_1) = \sum_{k=-\infty}^{\infty} j^{-k} \overline{a}_k(\overline{\rho}_1) e^{j[(\omega_0+k\alpha)t_1+k\phi_1]} \tag{40}$$

Thus using Equations (36), (37), (39) and (40), we obtain the backscattered fields,

$$E_z(\overline{\rho},\omega) = T_M \iint \sum_{k,m=-\infty}^{\infty} j^{-(k+m)} a_{\parallel k}(\overline{\rho}_1')J_m(\omega\rho_1'/c)e^{j(k+m)\phi_1'}$$
$$\cdot e^{-j[\omega-\omega_0-(k+m)\alpha]t_1'} \rho_1'd\rho_1'd\phi_1'dt_1' \quad , \tag{41}$$

$$H_z(\overline{\rho},\omega) = T_E \iint \sum_{k,m=-\infty}^{\infty} \frac{1}{2} j^{-(k+m-1)} a_{\perp k}(\overline{\rho}_1')J_m(\omega\rho_1'/c)e^{j(k+m)\phi_1'}$$
$$\cdot \left\{ e^{j\beta_1'} e^{-j[\omega-\omega_0-(k+m+1)\alpha]t_1'} - e^{-j\beta_1'} e^{-j[\omega-\omega_0-(k+m-1)\alpha]t_1'} \right\}$$
$$\rho_1'd\rho_1'd\phi_1'dt_1' \quad , \tag{42}$$

where $a_\parallel$ and $a_\perp$ are the components of $\overline{a}$ parallel and perpendicular to the z-axis, respectively. β_1' is the angle between $\overline{a}_\perp$ and the positive x_1-axis. Substitute $m=n-k$ into Equation (41) and $m=n-k\mp1$ into Equation (42) and carry out the integration over t_1',

$$E_z(\overline{\rho},\omega) = 2\pi \, T_M \iint \sum_{n=-\infty}^{\infty} j^{-n} \, \delta(\omega-\omega_0-n\alpha) \, e^{jn\phi_1'}$$

$$\cdot \sum_{k=-\infty}^{\infty} a_{\parallel k}(\overline{\rho}') J_{n-k}(\omega\rho_1'/c) \, \rho_1' d\rho_1' d\phi_1' \quad , \quad (43)$$

$$H_z(\overline{\rho},\omega) = 2\pi \, T_E \iint \sum_{n=-\infty}^{\infty} -\frac{j^{-n}}{2} \, \delta(\omega-\omega_0-n\alpha) \cdot \sum_{k=-\infty}^{\infty} a_{\perp k}(\overline{\rho}_1')$$

$$\cdot \left\{ e^{j[(n-1)\phi_1'+\beta_1']} J_{n-1-k}(\omega\rho_1'/c) + e^{j[(n+1)\phi_1'-\beta_1']} J_{n+1-k}(\omega\rho_1'/c) \right\}$$

$$\rho_1' d\rho_1' d\phi_1' \quad . \qquad (44)$$

The integrations in Equations (43) and (44) are over the entire circumference of the cylinder's cross-section. If the cross-section is an orthogonal polygon of N sides, then Equation (43) can be simplified,

$$E_z(\overline{\rho},\omega) = 2\pi \, T_M \iint \sum_{n=-\infty}^{\infty} j^{-n} \, \delta(\omega-\omega_0-n\alpha) \, e^{jn\phi_1'} \sum_{i=0}^{N-1} e^{ji\frac{2\pi}{N}n}$$

$$\cdot \sum_{k=-\infty}^{\infty} a_{\parallel k}(\overline{\rho}_1') \, J_{n-k}(\omega\rho_1'/c) \, \rho_1' d\rho_1' d\phi_1' \quad ,$$

$$(45)$$

where the integration is over one side of the polygon only. Since

$$\sum_{i=0}^{N-1} e^{ji\frac{2\pi}{N}n} = \sum_{m=-\infty}^{\infty} N \, \delta_{n,mN} \quad , \qquad (46)$$

where $\delta_{i,j}$ is a Kronecker delta, therefore Equation (45) reduces to

$$E_z(\overline{\rho},\omega) = 2\pi N \, T_M \iint \sum_{m=-\infty}^{\infty} j^{-mN} \, \delta(\omega-\omega_0-mN\alpha) \, e^{jmN\phi_1'}$$

$$\cdot \sum_{k=-\infty}^{\infty} a_{\parallel k}(\overline{\rho}_1') \, J_{mN-k}(\omega\rho_1'/c) \, \rho_1' d\rho_1' d\phi_1' \quad . \qquad (47)$$

Similarly, Equation (44) reduces to

20

$$H_z(\bar{\rho},\omega) = 2\pi N \; T_E \iint \sum_{m=-\infty}^{\infty} -\frac{j}{2}^{-mN} \delta(\omega-\omega_0-mN\alpha) \cdot \sum_{k=-\infty}^{\infty} a_{\perp k}(\bar{\rho}_1')$$

$$\cdot \left\{ \begin{array}{l} e^{j[(mN-1)\phi_1'+\beta_1']} \cdot J_{mN-1-k}(\omega\rho_1'/c) \\ \\ + e^{j[(mN+1)\phi_1'-\beta_1']} J_{m\sharp\sharp+1-k}(\omega\rho_1'/c) \end{array} \right\} \rho_1' d\rho_1' d\phi_1' \quad . \quad (48)$$

To solve Equations (47) and (48), we need to know the quantities $a_\parallel$ and $a_\perp$. Unfortunately these quantities cannot be easily found except for the case of a circular cylinder. For a circular cylinder with radius a [5]

$$a_{\parallel k}(\bar{\rho}_1) = \frac{-2}{\omega_0 \mu_0 \pi \rho_1} \; \frac{1}{H_k^{(2)}(\omega_0 \rho_1/c)} \; \delta(\rho_1-a) \quad , \quad (49)$$

$$a_{\perp k}(\bar{\rho}_1) = \frac{j2}{\pi \omega_0 \rho_1/c} \; \frac{1}{H_k^{(2)'}(\omega_0 \rho_1/c)} \; \delta(\rho_1-a) \quad , \quad (50)$$

which are independent of ϕ_1. Therefore $E_z(\bar{\rho},\omega)$ and $H_z(\bar{\rho},\omega)$ vanish except when m=0. This means that the fields scattered from a rotating circular cylinder have the same frequency as the incident wave. It is conjectured that for an orthogonal polygon-cylinder with a large number of sides, the $a_\parallel$ and $a_\perp$ will be close to those given in Equations (49) and (50) with the constant radius a replaced by the variable radius $a(\phi_1)$. Therefore we shall substitute Equations (49) and (50) into Equations (47) and (48) and obtain

$$E_z(\bar{\rho},\omega) = T_M \int \sum_{m=-\infty}^{\infty} N \; \delta(\omega-\omega_0-mN\alpha) e^{jmN\phi_1'} \sum_{k=-\infty}^{\infty} \frac{J_{mN-k}[\omega a(\phi_1')/c]}{H_k^{(2)}[\omega_0 a(\phi_1')/c]} \; d\phi_1' \quad , \quad (51)$$

$$H_z(\bar{\rho},\omega) = T_E \int \sum_{m=-\infty}^{\infty} N \; \delta(\omega-\omega_0-mN\alpha) e^{jmN\phi_1'} \sum_{k=-\infty}^{\infty} \frac{1}{H_k^{(2)'}[\omega_0 a(\phi_1')/c]}$$

$$\cdot \frac{1}{2j} \left\{ e^{j(\beta_1'-\phi_1')} J_{mN-1-k}[\omega a(\phi_1')/c] \right.$$

$$\left. + e^{-j(\beta_1'-\phi_1')} J_{mN+1-k}[\omega a(\phi_1')/c] \right\} d\phi_1' \quad , \quad (52)$$

where we have lumped all the factors nonessential for calculating the relative power density spectrum into T_M and T_E. The spectrum consists of spectral lines. A single spectral line is proportional to the square of

21

$$E_m = \left| \int_{-\pi/N}^{\pi/N} N \, e^{jmN\phi_1} \sum_{k=-\infty}^{\infty} \frac{J_{mN-k}[(\omega_0+mN\alpha)a(\phi_1)/c]}{H_k^{(2)}[\omega_0 a(\phi_1)/c]} \, d\phi_1 \right| \qquad (53)$$

or

$$H_m = \left| \int_{-\pi/N}^{\pi/N} N \, e^{jmN\phi_1} \sum_{k=-\infty}^{\infty} \frac{1}{H_k^{(2)'}[\omega_0 a(\phi_1)/c]} \cdot \left\{ \cos\phi_1 \, J_{mN-k}'[(\omega_0+mN\alpha)a(\phi_1)/c] \right. \right.$$

$$\left. \left. - j\sin\phi_1 \, \frac{(mN-k)}{(\omega_0+mN\alpha)a(\phi_1)/c} \, J_{mN-k}[(\omega_0+mN\alpha)a(\phi_1)/c] \right\} d\phi_1 \right| \quad ,$$

$$(54)$$

where we have assumed that the range of integration spans one side of the polygon and that $\beta_1 = \pi/2$.

With low incident frequencies, $\omega_0 a(\phi_1)/c \ll 1$. The arguments of the Bessel and Hankel functions in Equations (53) and (54) are very small. Thus the values of E_m and H_m decrease very fast as $|m|$ increases. This means that no significant spectrum spreading occurs with low incident frequencies.

On the other hand, with high incident frequencies, $\omega_0 \gg mN\alpha$ and $a(\phi_1) > \lambda_0$. The arguments of the Bessel and Hankel functions in Equations (53) and (54) are in the order of $\omega_D/2\alpha$, where ω_D is the Doppler angular frequency defined in Equation (27). If we plot the Bessel and the inverse of the Hankel functions with fixed arguments against the orders, we note that if the arguments are large, say > 10, then the values of the Bessel and the inverse of the Hankel functions decrease very fast when the orders become greater than the arguments. This is shown in Figures 12-15. Thus with high incident frequencies, we can properly truncate the summations in Equations (53) and (54) at $\pm[\omega_D/\alpha]$,

$$E_m = \left| \int_{-\pi/N}^{\pi/N} N e^{jmN\phi_1} \sum_{k=-[\omega_D/\alpha]}^{[\omega_D/\alpha]} \frac{J_{mN-k}[\omega_0 a(\phi_1)/c]}{H_k^{(2)}[\omega_0 a(\phi_1)/c]} \, d\phi_1 \right| \quad , \qquad (55)$$

$$H_m = \left| \int_{-\pi/N}^{\pi/N} N e^{jmN\phi_1} \sum_{k=-[\omega_D/\alpha]}^{[\omega_D/\alpha]} \frac{1}{H_k^{(2)'}[\omega_0 a(\phi_1)/c]} \right.$$

$$\left. \cdot \left\{ \cos\phi_1 \, J_{mN-k}'[\omega_0 a(\phi_1)/c] - j\sin\phi_1 \, \frac{mN-k}{\omega_0 a(\phi_1)/c} \, J_{mN-k}[\omega_0 a(\phi_1)/c] \right\} d\phi_1 \right| .$$
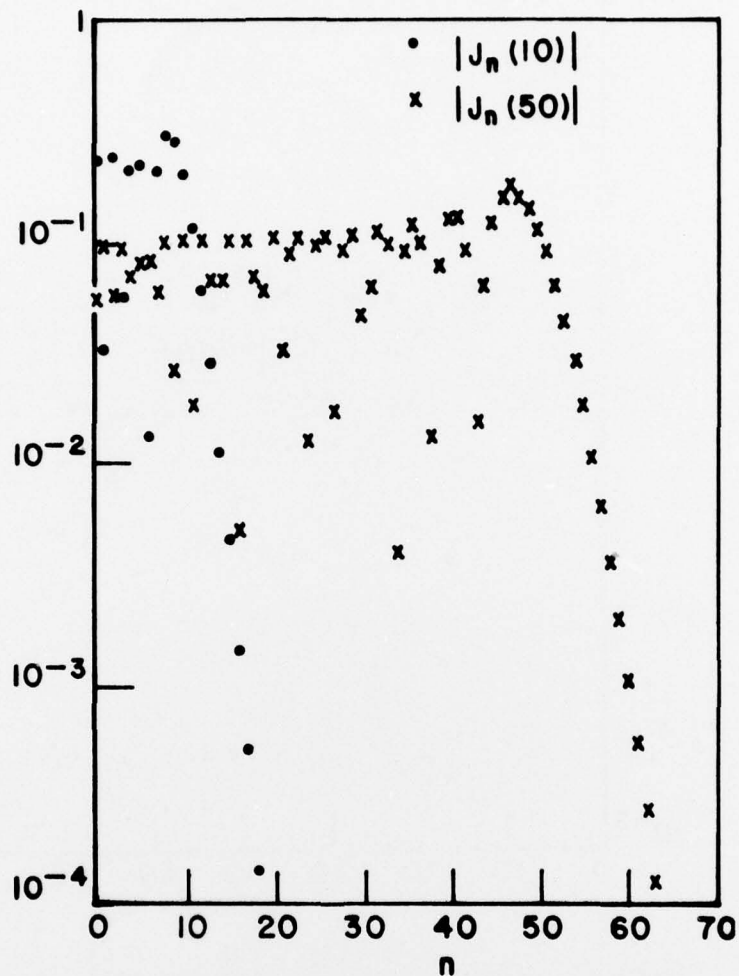
$$(56)$$

22

Figure 12. Plots of $|J_n(10)|$ and $|J_n(50)|$.

It can be easily shown from Equations (55) and (56) that in general $E_m \neq E_{-m}$ and $H_m \neq H_{-m}$. This means that the spectrum is generally not symmetric about m=0. A sufficient condition for the spectrum to be symmetric is $a(\phi_1)=a(-\phi_1)$ for $-\pi/N \leq \phi \leq \pi/N$, which can also be derived from Equations (55) and (56). For an orthogonal polygon-cylinder, this condition is certainly satisfied. Therefore the backscatter power density spectrum of an orthogonal polygon-cylinder is symmetric about m=0.
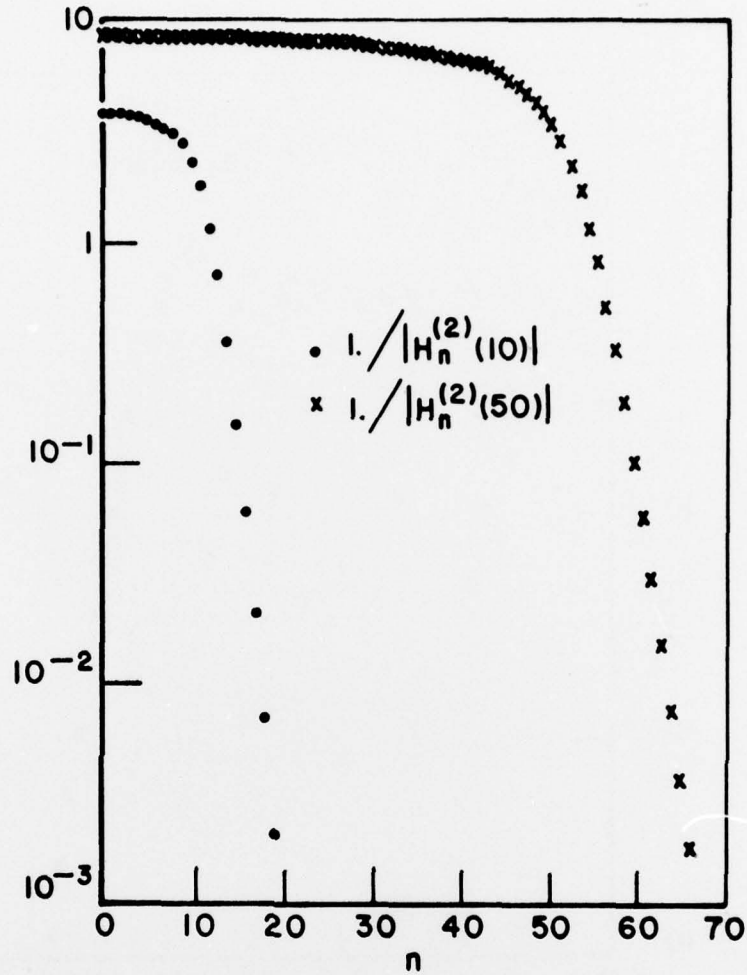
23

Figure 13. Plots of $\left|H_n^{(2)}(10)\right|^{-1}$ and $\left|H_n^{(2)}(50)\right|^{-1}$.

It is also obvious from the properties of the Bessel and Hankel functions with large arguments and large orders that the values of E_m and H_m are very small for $|m| > \omega_D/N\alpha$.

Table 1 shows the comparison of the power density spectra calculated using Equations (55) and (56) with those obtained in the last section. The agreement is very good. This not only substantiates the salient features of the backscatter power density spectrum of a large rotating cylinder established in the last section, but also indicates that the approximation of using Equations (49) and (50) for polygon-cylinders is indeed a good approximation.
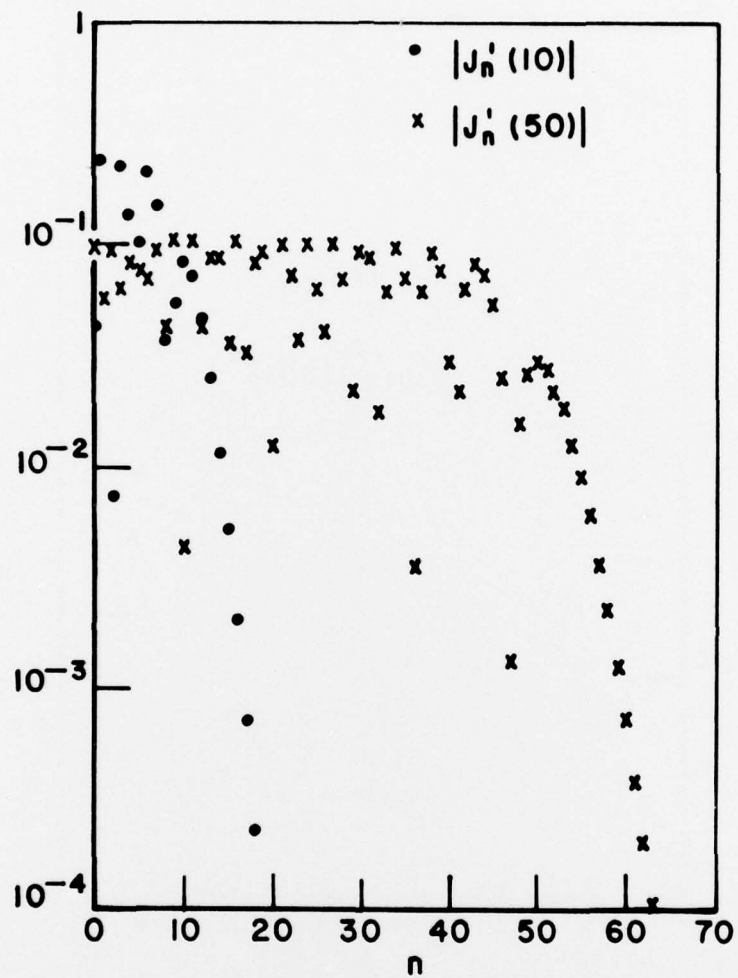
24

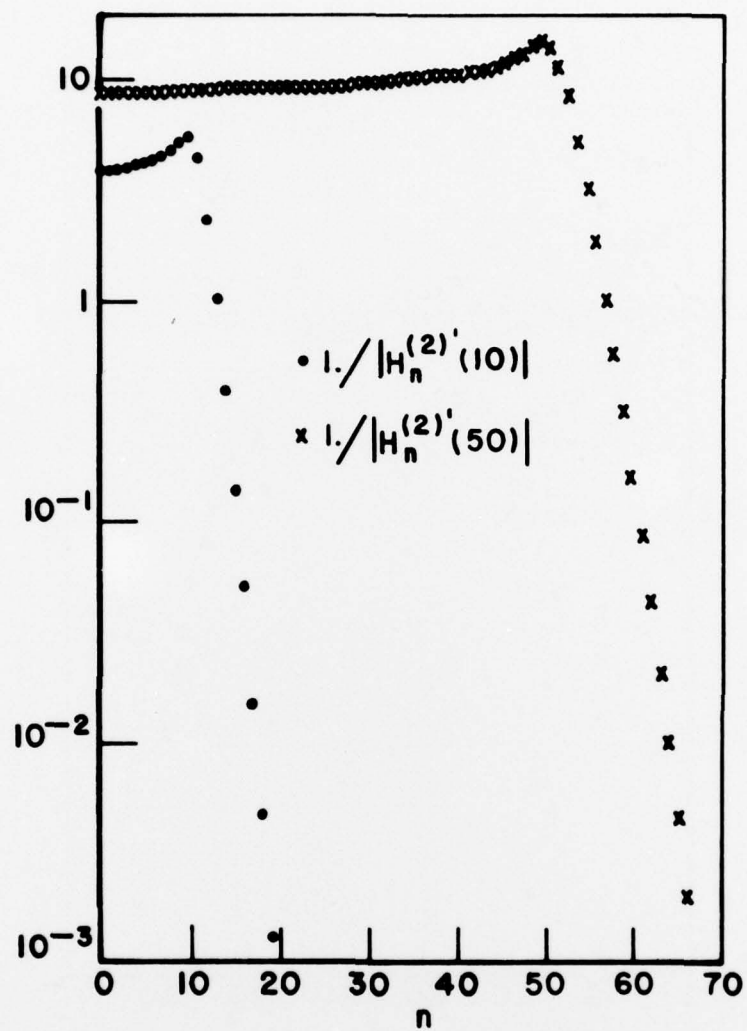Figure 14. Plots of $|J_n'(10)|$ and $|J_n'(50)|$.

25

Figure 15.   Plots of $\left|H_n^{(2)\prime}(10)\right|^{-1}$ and $\left|H_n^{(2)\prime}(50)\right|^{-1}$.

26

TABLE 1
COMPARISON OF THE POWER DENSITY SPECTRA

a = $5\lambda_0$, N = 10				
m	TM(dB)		TE(dB)	
0	0*	0	0*	0
1	- 2.5	- 2.6	- 2.4	- 2.5
2	- 9.9	-10.2	- 8.8	- 9.6
3	-17.7	-18.5	-15.6	-16.1
4	-24.7	-26.1	-19.4	-21.3
5	-31.1	-33.6	-23.9	-24.3
6	-39.7	-45.1	-20.4	-24.4
7	-62.7	-64.0	-40.0	-50.5
8				

a = $10\lambda_0$, N = 10				
m	TM(dB)		TE(db)	
0	- 4.0*	- 3.6	- 3.4*	- 3.4
1	- 0.9	- 0.8	- 0.8	- 0.7
2	- 0.8	- 0.9	- 0.7	- 0.8
3	- 4.5	- 4.8	- 4.2	- 4.4
4	- 9.7	-10.1	- 8.9	- 9.4
5	-14.9	-15.6	-13.6	-14.4
6	-19.6	-20.5	-17.5	-18.4
7	-23.8	-24.9	-20.2	-21.7
8	-27.4	-28.9	-23.1	-24.9
9	-30.8	-32.7	-23.8	-26.3
10	-34.1	-36.7	-26.0	-28.3
11	-37.7	-41.4	-25.5	-28.3
12	-42.1	-48.3	-21.5	-29.7
13	-55.9	-60.3	-31.5	-37.1

a = $10\lambda_0$, N = 20				
m	TM(dB)		TE(dB)	
0	+ 5.9*	+ 6.1	+ 6.1*	+ 6.1
1	- 3.9	- 3.8	- 3.4	- 3.5
2	-14.6	-14.7	-13.0	-13.8
3	-22.9	-23.1	-19.8	-20.8
4	-29.6	-30.1	-22.8	-25.8
5	-36.0	-37.3	-25.8	-28.7
6	-46.0	-48.6	-23.2	-29.6
7			-46.9	-72.8
8				

a = $5\lambda_0$, N = 20				
m	TM(dB)		TE(dB)	
0	+ 3.6*	+ 3.7	+ 3.8*	+ 3.8
1	-13.0	-13.0	-11.4	-12.1
2	-26.6	-27.2	-20.4	-22.3
3	-43.1	-45.4	-22.7	-24.4

* GTD solutions

27

IV. CONCLUSIONS

In this report, two methods for calculating the power density spectra of the scattered fields from a large rotating conducting cylinder are presented. Results obtained using these two methods agree very well with each other.

The backscatter power density spectrum of a rotating cylinder with arbitrary cross section consists of discrete spectral lines. For an orthogonal polygon-cylinder, the spectrum has the following interesting features:

(1) It is symmetric about the incident angular frequency.

(2) For the TM case, the spectrum decreases monotonically. However, for the TE case, it has local maxima around $\omega \pm \omega_D$, where ω_D is the Doppler angular frequency.

(3) The spectrum is essentially confined to a bandwidth $\omega_0 - \omega_D < \omega < \omega_0 + \omega_D$.

(4) The near-field spectrum is essentially the same as the far-field spectrum.

REFERENCES

1.   A. Sommerfeld, <u>Electrodynamics</u>, Academic Press, New York, 1952.

2.   N. Wang, "Self-consistent GTD Formulation for Conducting Cylinders With Arbitrary Convex Cross Section," IEEE Trans., AP-24, (1976), p. 463.

3.   R.G. Kouyoumjian and P. Pathak, "A Uniform Geometrical Theory of Diffraction for an Edge in a Perfectly Conducting Surface," Proc. IEEE, vol. 62, (1974), p. 1448.

4.   A. Papoulis, <u>The Fourier Integral and Its Applications</u>, McGraw-Hill, New York, 1962.

5.   R.F. Harrington, <u>Time-Harmonic Electromagnetic Fields</u>, McGraw-Hill, New York, 1961.